Supporting Information

Inherent Anti-Fenton Property of Single-Atom Rhenium for Ultra-Durable Oxygen Reduction Reaction

Xin-Zheng Yue[b], Yun-Ce Liu[b], Bang-An Lu[a], Xin Du[b], Wen Lei[b], Zhong-Yi Liu[b], Sha-Sha Yi[a,*], and Chao Lu[b,c,*]

[a]School of Materials Science and Engineering, Zhengzhou University, Zhengzhou 450001, China.

[b]College of Chemistry, Zhengzhou University, Zhengzhou 450001, China.

[c]State Key Laboratory of Chemical Resource Engineering, Beijing University of Chemical Technology, Beijing 100029, China

Corresponding authors:

E-mail addresses: yiss@zzu.edu.cn; luchao@mail.buct.edu.cn

Table of Contents

4. Experimental section.....S4
Figure S1. Binding energies of M-N_4 structures (M = Mn, Fe, Co, Ni, Ru, Re, Pt, Ir, Cu and Zn). S10
Figure S2. FESEM images of (a) ZIF-8, (b) ReO_4^-/ZIF-8, (c) N-C, and (d) Re-SAC. S10
Figure S3. EDX spectrum of Re-SAC. S11
Figure S4. XRD patterns of ZIF-8 and ReO_4^-/ZIF-8. .....S11
Figure S5. FTIR spectra of ZIF-8 and ReO_4^-/ZIF-8, whereas the four peaks at 419, 1580, 2929, and 3450 cm^{-1} are labeled as Zn-N, C=N, C-H, and -OH bonds, respectively. S12
Figure S6. Raman spectra of Re-SAC-900 and Re-SAC-800. .....S12
Figure S7. a) Survey and b) high-resolution Re 4f XPS spectra of Re-SAC.....S13
Figure S8. RDE polarization curves of Re-SAC, Re-SAC-900, and Re-SAC-800. .....S13
Figure S9. Survey XPS spectrum of Re-SAC after RDE tests (inset shows Pt 4f XPS spectrum of Re-SAC).....S14
Figure S10. Comparison of the TOF values and mass activities (MA) of Re-SAC and Pt/C. S14
Figure S11. Polarization curves of Re-SAC with various rotation speeds. S15
Figure S12. Koutecky-Levich plots of Re-SAC at different potentials. S15
Figure S13. Polarization curves of (a) N-C and (b) Pt/C measured in O_2-saturated 0.1 M KOH aqueous solution at various rotation speeds. The corresponding Koutecky-Levich plots of (c) N-C and (d) Pt/C at different potentials. S16
Figure S14. H_2O_2 yield and electron transfer number (n) calculated from RRDE measurements of Re-SAC and N-C. S16
Figure S15. Voltammograms recorded at various rotation speeds using RRDE: (a) no catalyst loading and (b) Re-SAC loading. The loading mass of Re-SAC was 0.09 mg cm^{-2}. S17
Figure S16. The *i-t* chronoamperometric response of Re-SAC and Pt/C at 0.6 V in O_2-saturated solution at a rotation rate of 1600 rpm. S17
Figure S17. Galvanostatic polarization test of Re-SAC at -5 mA cm^{-2} in O_2-saturated 0.1 M KOH solution at a rotation speed of 1600 rpm. S18
Figure S18. a) XRD patterns of Re-SAC before and after 10000 CV cycles. b) TEM image and c) EDX elemental mapping images of Re-SAC after 10000 CV cycles. S19
Figure S19. (a) C 1s, (b) N 1s, and (c) Re 4f XPS spectra of Re-SAC after 10000 CV cycles S19
Figure S20. CV curves of (a) Re-SAC, (b) Pt/C and (c) N-C measured in the potential range of 0.76-0.86 V *vs.* RHE at different scan rates. (d) The capacitive current density as a function of scan rates for N-C, Re-SAC, and Pt/C. S20
Figure S21. EIS plots of Re-SAC, N-C, and Pt/C. Inset shows the fitted equivalent circuit model.....S20
Figure S22. Photograph of a ZAB with measured open-circuit voltage using Re-SAC as the air cathode catalyst. S21
Figure S23. Comparison of the power energy between Re-SAC and the catalysts reported recently.....S21
Figure S24. Digital photograph of a commercial color LED (blue, red, and green) lit by two-series-connected Re-SAC-based home-made ZAB.....S22
Figure S25. The optimized structure diagrams of (a) Re-SAC and (b) N-C. S22
Figure S26. COHP for the M-N (M = Fe or Re) bond in Re-SAC and Fe-SAC. S22
Figure S27. The calculated pDOS of C 2p and Re 5d for Re-SAC. S23
Table S1. BET surface area, micropore sufface area and mesopore area of Re-SAC and N-C catalysts.S24

Table S2. Structural parameters extracted from the Re L_3-edge EXAFS fitting (S_0^2 = 0.899).....S24
Table S3. The ORR performance comparison of Pt/C in this work with the reported values in literature. S25
Table S4. ORR performance comparison of Re-SAC with other highly active catalysts reported recently. S26
Table S5. Collection efficiency determined by voltammograms recorded at various rotation speeds using RRDE.....S27
Supplementary references.....S28

4. Experimental section

4.1 Reagents and materials

Zinc nitrate hexahydrate ($Zn(NO_3)_2·6H_2O$, 99%), 2,20-Azinobis (3-ethylbenzthiazoline-6-sulfonate) (ABTS), 2-methylimidazole ($C_4H_6N_2$, 98%), and Nafion solution (5 wt%) were purchased from Aladdin. Methanol (CH_3OH, 99.5%) was bought from Tianjin Kermel Chemical Reagent Co., Ltd. Ammonium perrhenate (NH_4ReO_4, 99.99%) was purchased from Shanghai D&B Biological Science and Technology Co., Ltd. Sulfuric acid (H_2SO_4, 95%~98%) was bought from Luoyang Chemical Reagent Plant. Potassium hydroxide (KOH, 85%) was purchased from Sinopharm Chemical Reagent Co., Ltd. Commercial 20 wt% Pt/C was purchased from Alfa Aesar Co., Ltd. N_2/H_2 mixture gas (20 vol% of H_2) and O_2 (99.999%) were supplied by Henan Yuanzheng Special Gas Co., Ltd. Deionized water (18.2 MΩ·cm) was prepared in the laboratory with an ultrapure purification system (Smart-S150).

4.2 Synthesis of ReO_4^-/ZIF-8 and ZIF-8

2.6280 g of $C_4H_6N_2$ was dissolved in 30 mL of methanol to obtain solution A. Solution B was achieved by mixing 2.3800 g of $Zn(NO_3)_2·6H_2O$ and 0.3353 g of NH_4ReO_4 in 60 mL of methanol. Subsequently, solution B was quickly poured into the solution A under stirring at room temperature and maintained for 12 h. After centrifugation and washing with methanol, the resulting precipitate was dried at 70℃ overnight in a vacuum oven, labeling as ReO_4^-/ZIF-8. Similarly, ZIF-8 was also synthesized without adding NH_4ReO_4.

4.3 Synthesis of Re-SAC and N-C

The as-prepared ReO_4^-/ZIF-8 was put into a tubular furnace and heated at 900°C for 2 h in

H_2/Ar atmosphere at a ramping rate of 5°C min^{-1}. After naturally cooling down to room temperature, the resultant powders were washed in a 0.5 M H_2SO_4 solution at 80°C for 10 h. After fully drying, the product was heated in an H_2/Ar atmosphere at 800, 900, and 1000°C for 2 h (a heating rate of 5°C min^{-1}), respectively. The final sample was denoted as Re-SAC-*x*, in which *x* represents the heating temperature (800, 900, and 1000°C). The Re-SAC-1000 was designated as Re-SAC unspecified. For comparison, N-C was also prepared by a method similar to that of Re-SAC-*x*, using ZIF-8 as the precursor. The characterizations, electrochemical measurements, ZAB assembly and theoretical calculations are provided in the Supporting Information.

4.4 Characterization

X-ray diffraction (XRD) measurements were characterized on a D/Max-2500 X-ray diffractometer with Cu Kα radiation. Raman spectra were analyzed using a 532 nm laser on a Reinshawin Via reflectometric micro-Raman spectrometer. Fourier transform infrared spectroscopy (FTIR) was conducted on the Tensor27 (Bruker) FTIR spectrometer in the spectral window range of 500~4000 cm^{-1}. X-ray photoelectron spectroscopy (XPS) was collected using Al Kα as an exciting radiation source on a Thermo VG Scientific ESCALAB 250 spectrometer. The X-ray absorption fine structure (XAFS) spectroscopy was acquired at the 16BM-D station of the High-Pressure Collaborative Access Team (HPCAT) at the Advanced Phonon Source of Argonne National Laboratory. The fourier transform extended XAFS (FT-EXAFS) raw data were processed and fitted with the program Athena. The field emission scanning electron microscopy (FESEM) was performed by the JSM-6490LV. Transmission electron microscopy (TEM), high-resolution TEM (HRTEM), and energy-dispersive X-ray (EDX) spectroscopy elemental analyses were obtained via a JEOL JEM-2100 with a field emission gun of 200 kV. The high-angle annular dark-field scanning TEM

(HAADF-STEM) images were obtained from a FEI Titan Cubed Themis G2 300 equipped with a probe spherical aberration corrector. Inductively coupled plasma optical emission spectrometry (ICP-OES) was conducted on SHIMADZU. For the ICP-OES test, 0.1 mg of Re-SAC was added to 1 mL of concentrated HNO_3. After complete dissolution of Re, the solution was diluted to 100 mL and filtered to obtain a clear and transparent solution. Finally, 10 mL of the filtrate was used for subsequent testing. Inductively coupled plasma-mass spectrometry (ICP-MS) was performed on an Agilent 7850 instrument. Ultraviolet-visible absorption spectra were characterized by UV-1600PC UV-vis spectrophotometer.

4.4 Electrochemical measurements

Electrocatalytic oxygen evolution reaction (ORR) measurements were conducted on an electrochemical workstation (RST5810F, Inc., Zhengzhou) at ambient conditions using a rotating disk electrode (RDE) with a glassy carbon (GC) disk of 4 mm in diameter as the working electrode, Ag/AgCl (3.5 M KCl solution) as the reference electrode, and Pt foil as the counter electrode. The working electrode was prepared as follows: 1.2 mg of catalysts were dispersed into 1 mL of ethanol and 50 μL of Nafion solution, followed by ultrasonication for 30 min to form a homogeneous ink. Then, 10 μL of ink solution was dropped on the RDE and dried naturally. The loading mass of catalyst was calculated to be 0.09 mg cm^{-2}. The electrolyte is 0.1 M KOH. Before the ORR tests, the electrolyte was bubbled with high-purity O_2 or N_2 for 1 h. All measured potentials (*vs.* Ag/AgCl) were converted to the reversible hydrogen electrode (RHE) by the following formula: $E_{RHE} = E_{Ag/AgCl} + 0.963$ V.

Polarization curves were recorded at a scan rate of 10 mV s^{-1}. The Tafel plots were acquired from polarization curves according to the Tafel equation ($\eta = b\log|j| + a$, where *j,* b, and a are the

current density, Tafel slope, and intercept, respectively). ORR activities were tested in O_2-saturated 0.1 M KOH at different rotation rates with a sweep rate of 10 mV s^{-1}. Cyclic voltammetry (CV) curves were measured in N_2- and O_2-saturated 0.1 M KOH solutions at a scan rate of 10 mV s^{-1}. To achieve double layer capacitance (C_{dl}), CV curves were recorded at various scan rates (10, 20, 30, 40, and 50 mV s^{-1}) in the potential range of 0.76~0.86 V *vs.* RHE. Electrochemical impedance spectroscopy (EIS) measurements were conducted in a 0.1 M KOH solution, with the frequency ranging from 10^5 to 0.1 Hz and an amplitude of 7 mV. The ORR stability was tested by CV measurement at 0.6~1.0 V *vs.* Ag/AgCl with a scan rate of 50 mV s^{-1} and chronoamperometry at a constant potential of 0.60 V *vs.* Ag/AgCl for 10 h. For the stability test, O_2 was bubbled into a 0.1 M KOH electrolyte for 1 h prior to the experiment, and a continuous flow of O_2 was maintained over the electrolyte during the test to ensure O_2 saturation. Kinetic current density was determined by the Koutecky-Levich equation (S1):

$$j^{-1} = j_L^{-1} + j_k^{-1} = B^{-1}\omega^{1/2} + j_k^{-1} \quad \text{(S1)}$$

where j is the measured current density (mA cm^{-2}), j_k and j_L are the kinetic and diffusion-limited current densities (mA cm^{-2}), respectively, ω is the angular velocity of the disk (rpm).

The turn-over frequency (TOF) can be estimated as follows:

$$\text{TOF} = \frac{j_k * N_e}{\omega * c * N_A / M} \quad \text{(S2)}$$

where j_k is the kinetic current density (mA cm^{-2}), N_e is the electron number per Coulomb (6.24×10^{18}), ω is the metal content in the catalyst , c is the catalyst loading on the electrode (0.09 mg cm^{-2}), N_A is the Avogadro constant (6.02×10^{23}), and M is the molar mass of Re (186.20 g mol^{-1}).

Rotating ring-disk electrode (RRDE) measurements were performed at a scan rate of 10 mV s^{-1}

at 1600 rpm, and the ring electrode voltage was kept at 1.3 V *vs.* RHE. The electron transfer number (n) and H_2O_2% were determined by the following equations (S3,S4):

$$n = 4 * \frac{i_D}{i_D + i_R / N} \quad \text{(S3)}$$

$$H_2O_2\% = 200 * \frac{i_R / N}{i_D + i_R / N} \quad \text{(S4)}$$

where i_D and i_R are the disk current and ring current (mA cm^{-2}), respectively. The H_2O_2 collection coefficient (N) at the ring was 0.37.

4.6 Zinc-air battery assembly

A zinc-air battery (ZAB) consists of Re-SAC coated carbon paper (with a mass loading of 1.0 mg cm^{-2}) as the air cathode, a Zn plate as the anode, and 6.0 M KOH and 0.2 M $Zn(CH_3COO)_2$ aqueous solution as the electrolyte. The cathode catalysts utilized in the circulating charge and discharge tests consisted of Re-SAC or 20 wt% Pt/C blended with commercial RuO_2 at a mass ratio of 1:1. The ZABs tests were conducted under standard atmospheric conditions.

4.7 Theoretical calculations

The Vienna ab-initio simulation package (VASP) was employed to conduct density functional theory (DFT) calculations. A generalized gradient approximation (GGA) in the Perdew-Burke-Ernzerhof (PBE) form was employed, along with a cutoff energy of 400 eV for the plane-wave expansion set. Electron-ion interactions were described using projector augmented-wave (PAW) potentials. Monkhorst-Pack grids (k-points of 3×3×1) were selected for structural optimization and frequency calculation, while 9×9×1 grids were used for more accurate electronic structure calculations. A vacuum slab of 15 Å in the z-direction was used to avoid the interaction between the period layers. Electronic energy minimization tolerance was set at 10^{-4} eV. By using the optB88

correction method, van der Waals interactions were taken into account. Geometrical visualizations were performed using the VESTA program package. The free energy changes for each elementary step were calculated using the computational hydrogen electrode (CHE) method, an innovative technique pioneered by Norskov and his colleagues. The Gibbs free energy change (ΔG) can be defined as the difference between the free energies of the final and initial states, using the formula (S5) as follows:

$$\Delta G = \Delta E + \Delta ZPE - T\Delta S + \Delta G_{U} + \Delta G_{pH} \quad \text{(S5)}$$

where ΔE and ΔZPE are the adsorption energy calculated based on DFT calculations and the zero-point energies correction, respectively. T is the temperature (298.15 K), and ΔS is the entropy change. ΔG_{U} and ΔG_{pH} are the contributions to the free energy due to the change of the electrode potential (U) and the pH value, respectively. $\Delta G_{U} = -neU$, where n is the number of transferred electrons. From a thermodynamic perspective, a positive ΔG indicates the presence of an energy barrier and necessitates an additional voltage to drive the process, whereas a negative value denotes spontaneous reaction progression.

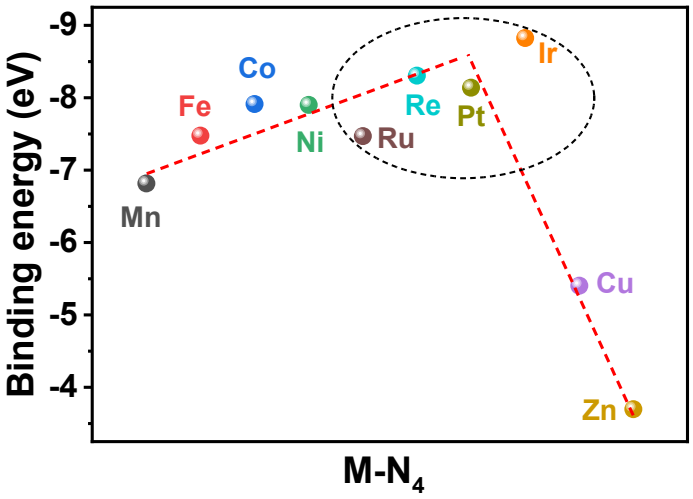

Figure S1. Binding energies of M-N_4 structures (M = Mn, Fe, Co, Ni, Ru, Re, Pt, Ir, Cu and Zn).

As shown in Figure S1, the binding energy of Re-N_4 configuration (−8.306 eV) is significantly more negative than other M-N_4 configurations (where M represents Mn, Fe, Co, Ni, Ru, Pt, Cu, and Zn).

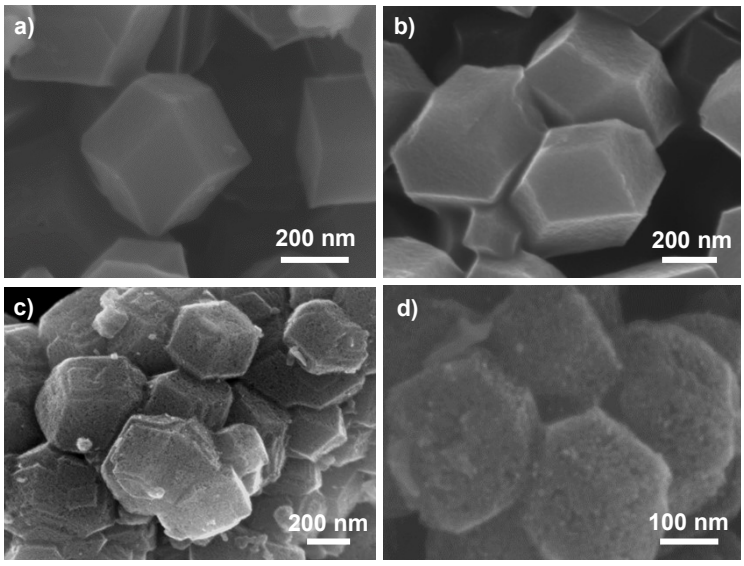

Figure S2. FESEM images of (a) ZIF-8, (b) ReO_4^-/ZIF-8, (c) N-C, and (d) Re-SAC.

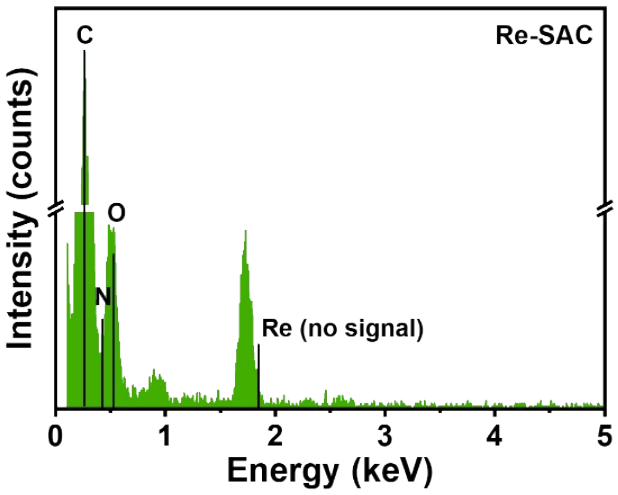

Figure S3. EDX spectrum of Re-SAC.

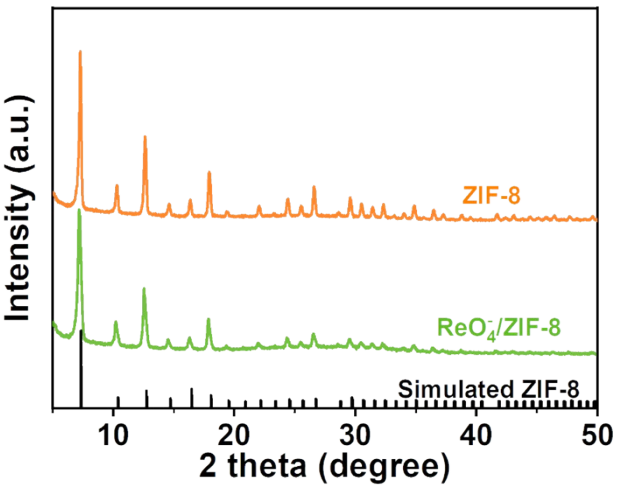

Figure S4. XRD patterns of ZIF-8 and ReO_4^-/ZIF-8.

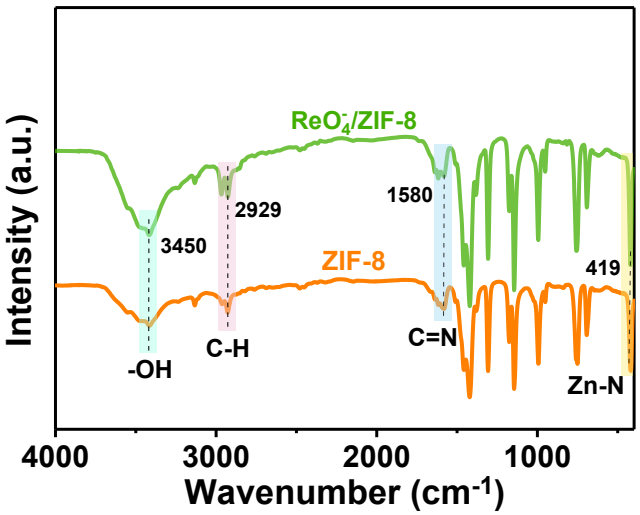

Figure S5. FTIR spectra of ZIF-8 and ReO_4^-/ZIF-8, whereas the four peaks at 419, 1580, 2929, and 3450 cm^{-1} are labeled as Zn-N, C=N, C-H, and -OH bonds, respectively.

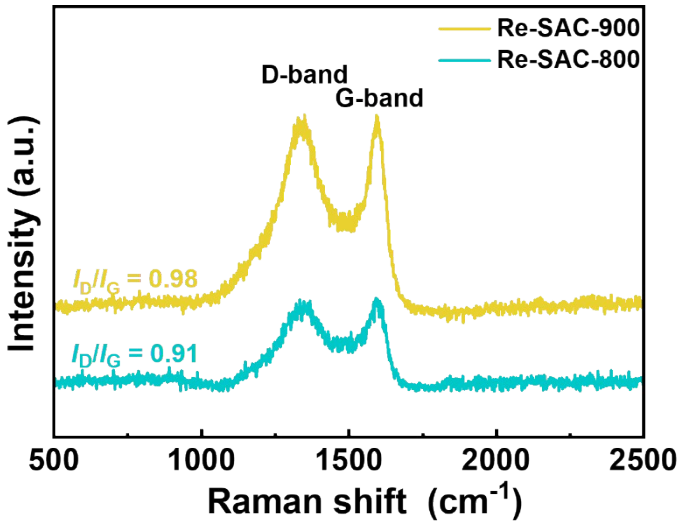

Figure S6. Raman spectra of Re-SAC-900 and Re-SAC-800.

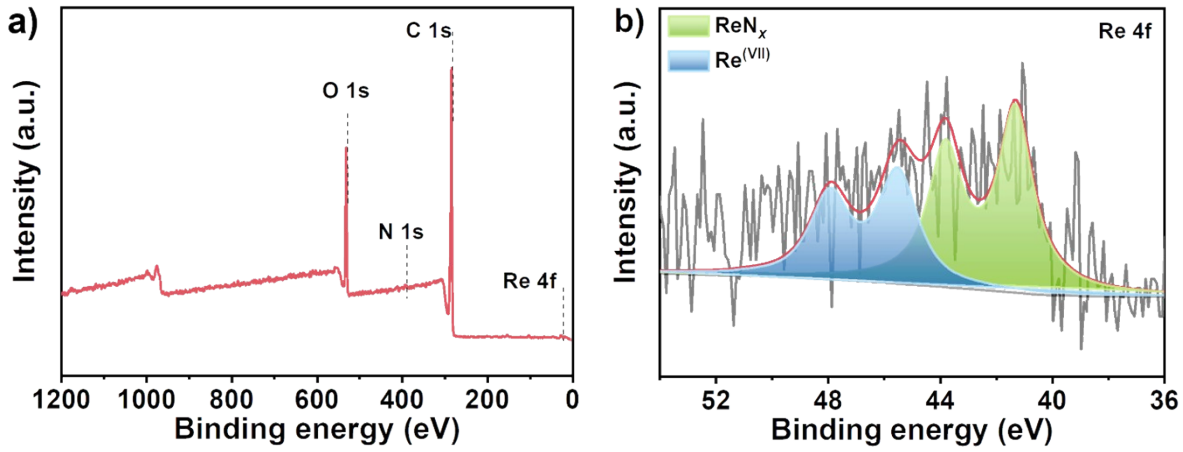

Figure S7. a) Survey and b) high-resolution Re 4f XPS spectra of Re-SAC.

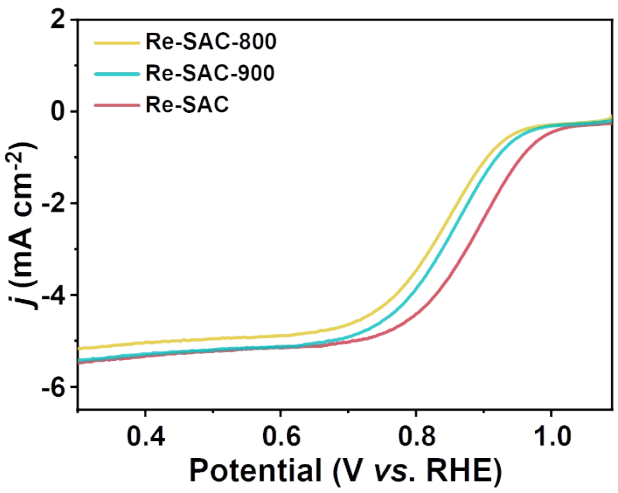

Figure S8. RDE polarization curves of Re-SAC, Re-SAC-900, and Re-SAC-800.

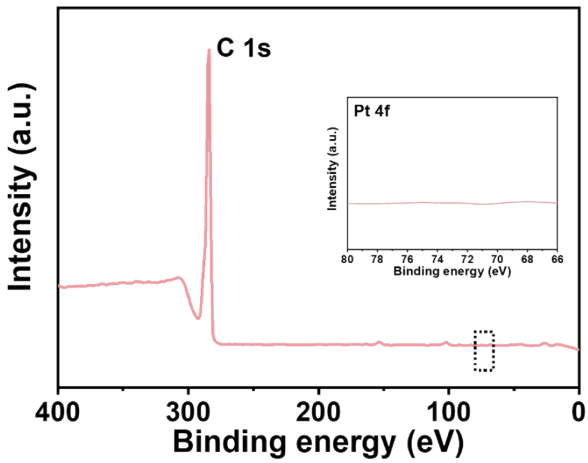

Figure S9. Survey XPS spectrum of Re-SAC after RDE tests (inset shows Pt 4f XPS spectrum of Re-SAC).

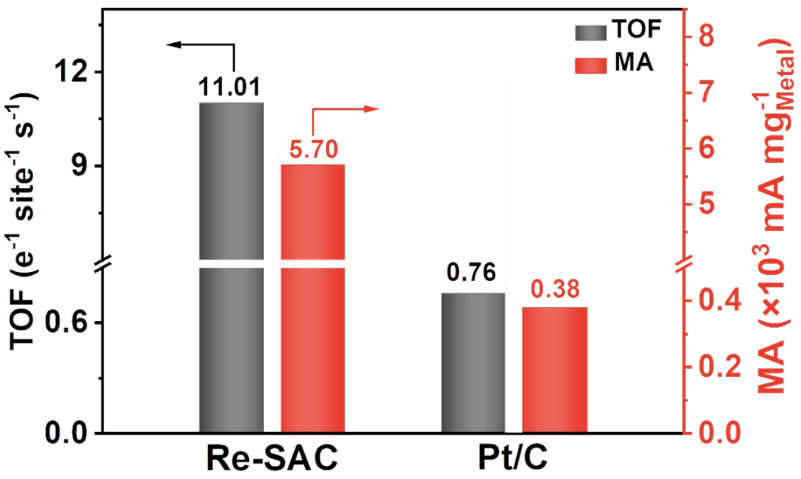

Figure S10. Comparison of the TOF values and mass activities (MA) of Re-SAC and Pt/C.

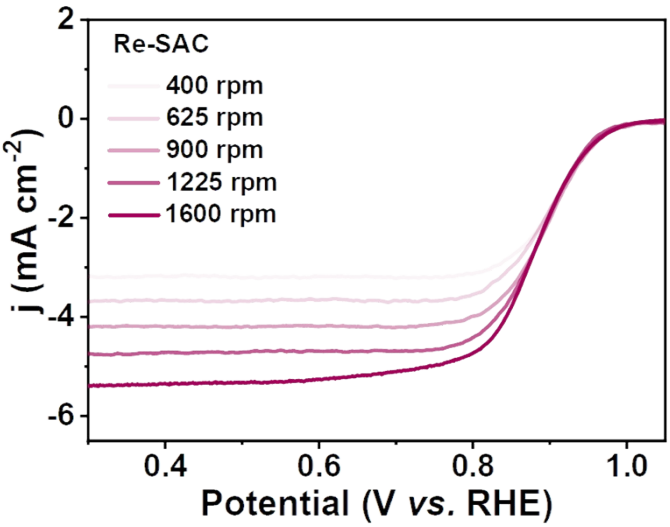

Figure S11. Polarization curves of Re-SAC with various rotation speeds.

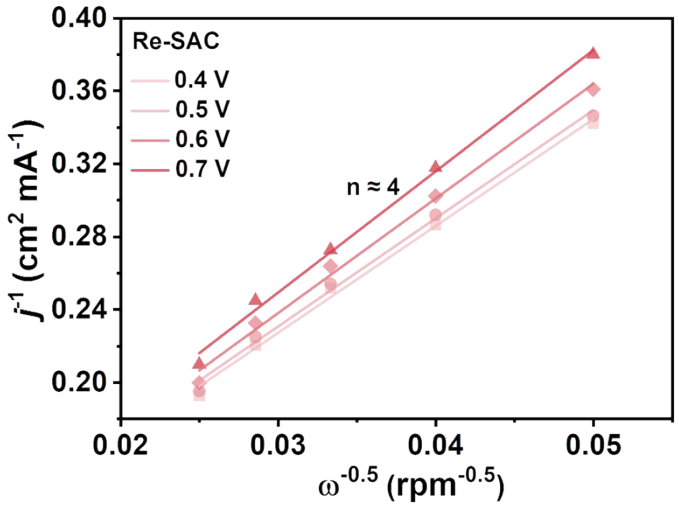

Figure S12. Koutecky-Levich plots of Re-SAC at different potentials.

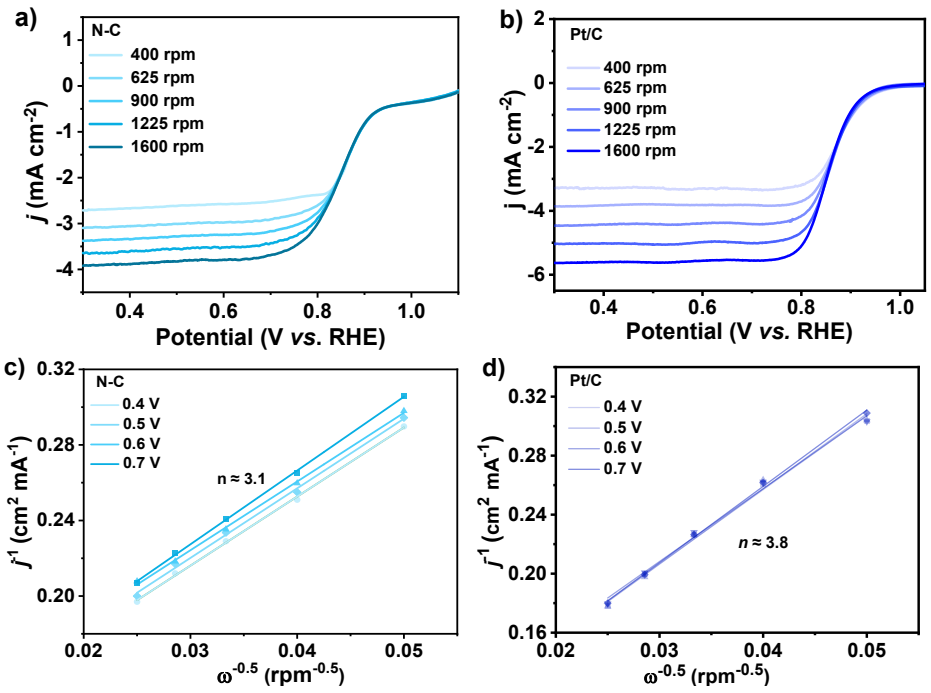

Figure S13. Polarization curves of (a) N-C and (b) Pt/C measured in O_2-saturated 0.1 M KOH aqueous solution at various rotation speeds. The corresponding Koutecky-Levich plots of (c) N-C and (d) Pt/C at different potentials.

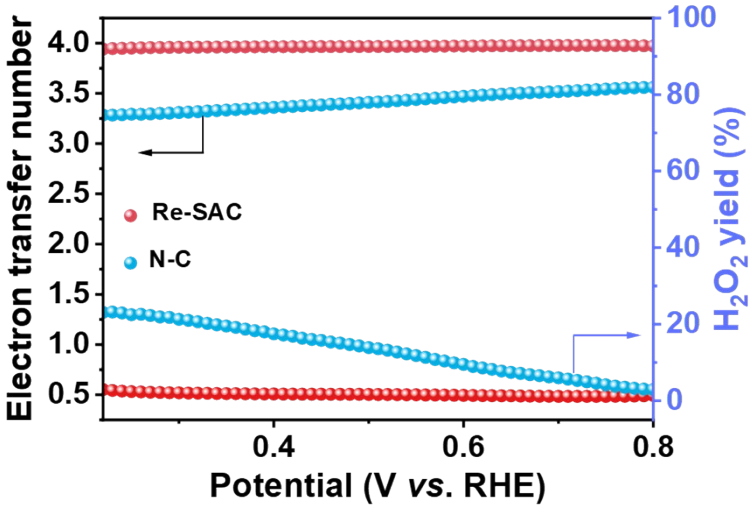

Figure S14. H_2O_2 yield and electron transfer number (n) calculated from RRDE measurements of Re-SAC and N-C.

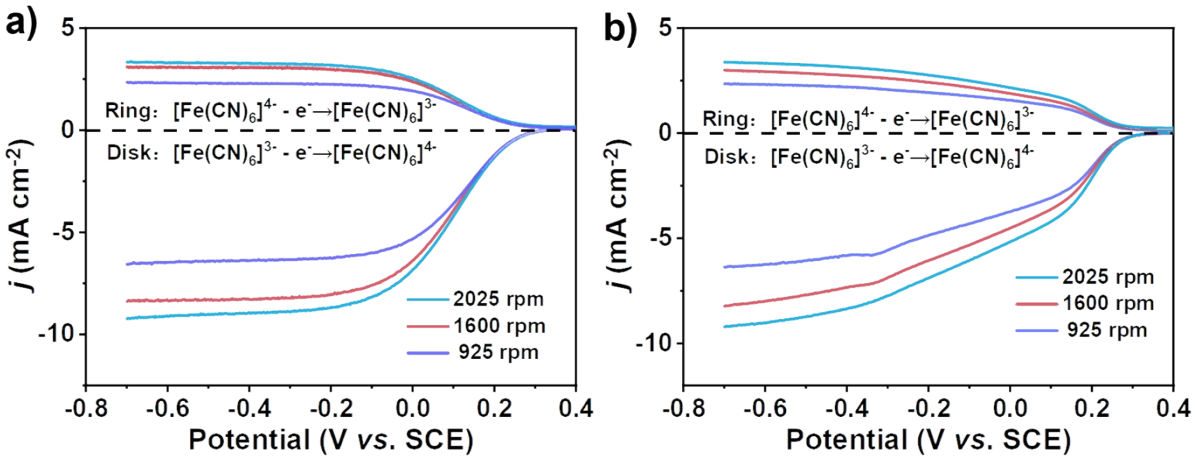

Figure S15. Voltammograms recorded at various rotation speeds using RRDE: (a) no catalyst loading and (b) Re-SAC loading. The loading mass of Re-SAC was 0.09 mg cm^{-2}.

The RRDE was immersed in a mixture solution of $K_3Fe(CN)_6$ (10 mM) and 1.0 M KNO_3. A potential range of 0.5~-0.7 V *vs.* SCE was applied to the disk electrode, while maintaining a constant potential of 0.7 V *vs.* SCE at the ring electrode. The ring-disk currents were performed at various rotation speeds, and the collection efficiency (N) was calculated using equation (S6):

$$N_{empirical} = -\frac{i_{Ring}}{i_{Disk}} \quad \text{(S6)}$$

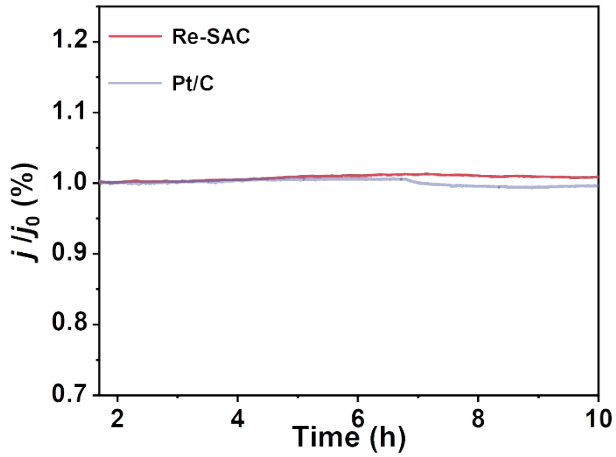

Figure S16. The *i-t* chronoamperometric response of Re-SAC and Pt/C at 0.6 V in O_2-saturated solution at a rotation rate of 1600 rpm.

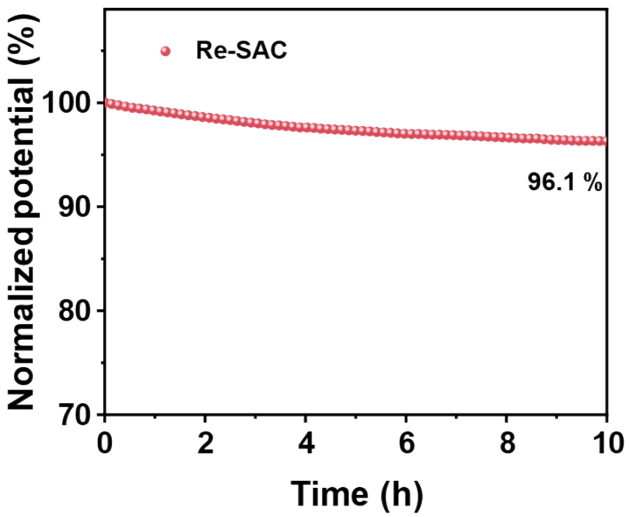

Figure S17. Galvanostatic polarization test of Re-SAC at -5 mA cm^{-2} in O_2-saturated 0.1 M KOH solution at a rotation speed of 1600 rpm.

To investigate whether the active centers of Re are lost or dissolved during the galvanostatic polarization test, we performed ICP-OES analysis on Re-SAC. The relative content of dissolved Re element in the electrolyte, as compared to the original sample, is defined as the proportionate loss of Re. The relative content can be estimated using equation (S7)[S1]:

$$Relative\ content = \frac{C_d * V}{C_0 * m} \quad \text{(S7)}$$

where C_d is the dissolved concentration of the Re element (mg L^{-1}), V is the volume of electrolyte (L), C_0 is the original loading content of the Re on the electrode (mg kg^{-1}), and m is the mass of electrode (kg).

As a result, a relative content of dissolved Re at only 5.13% was determined, demonstrating the excellent stability of Re-SAC.

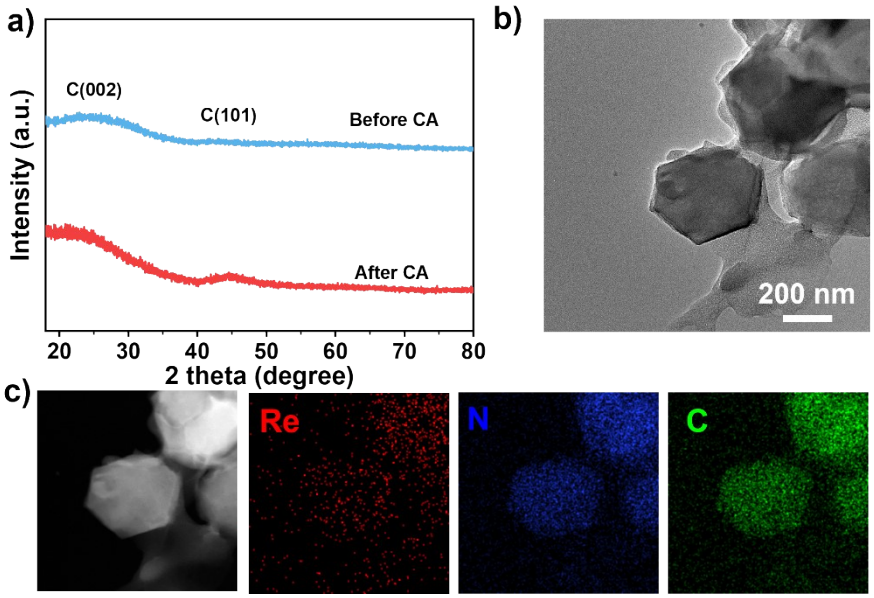

Figure S18. a) XRD patterns of Re-SAC before and after 10000 CV cycles. b) TEM image and c) EDX elemental mapping images of Re-SAC after 10000 CV cycles.

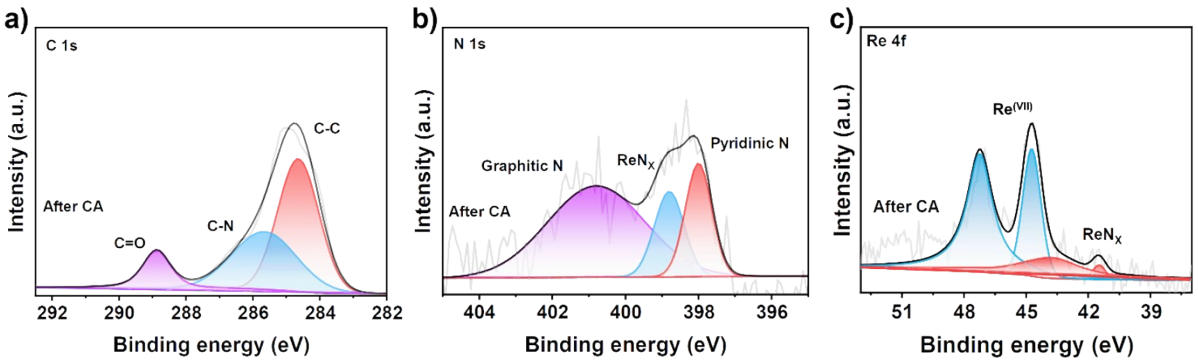

Figure S19. (a) C 1s, (b) N 1s, and (c) Re 4f XPS spectra of Re-SAC after 10000 CV cycles .

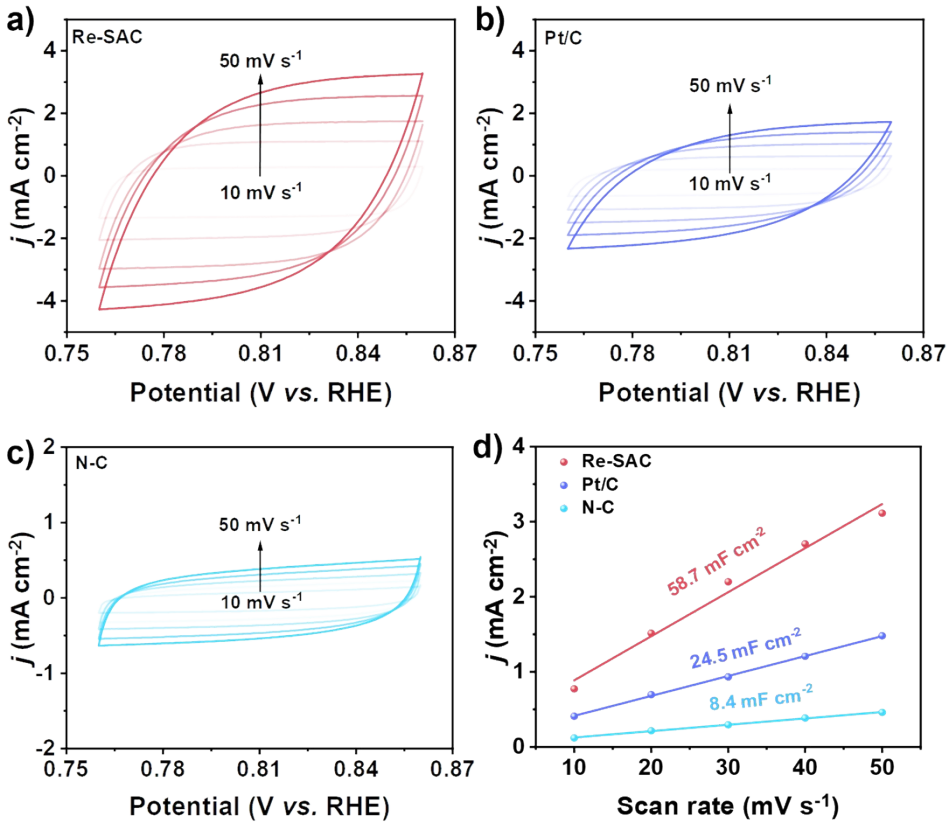

Figure S20. CV curves of (a) Re-SAC, (b) Pt/C and (c) N-C measured in the potential range of 0.76-0.86 V *vs.* RHE at different scan rates. (d) The capacitive current density as a function of scan rates for N-C, Re-SAC, and Pt/C.

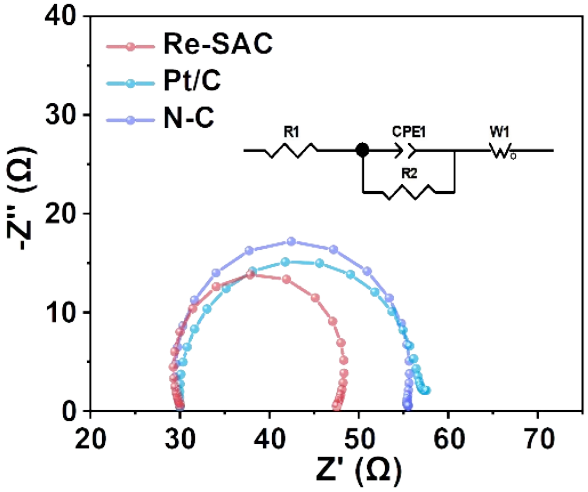

Figure S21. EIS plots of Re-SAC, N-C, and Pt/C. Inset shows the fitted equivalent circuit model.

In the electrical equivalent circuit model, R1 represents the total ohmic resistance of the solution, R2 denotes the charge-transfer resistance of the electrodes, CPE1 corresponds to the constant phase element related to the double layer capacity, and W1 is the generalized finite Warburg impedance of the solid-phase diffusion.

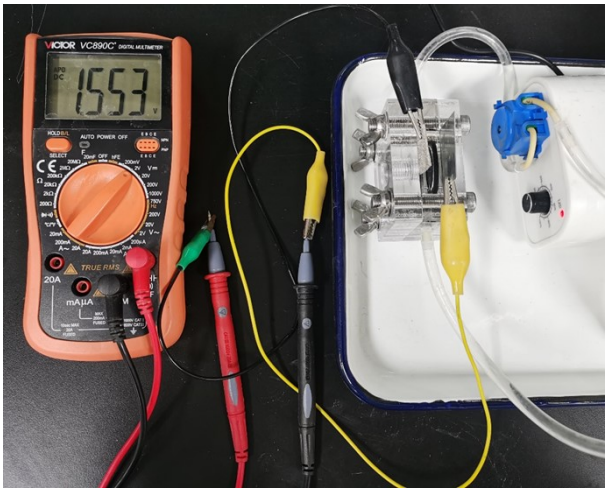

Figure S22. Photograph of a ZAB with measured open-circuit voltage using Re-SAC as the air cathode catalyst.

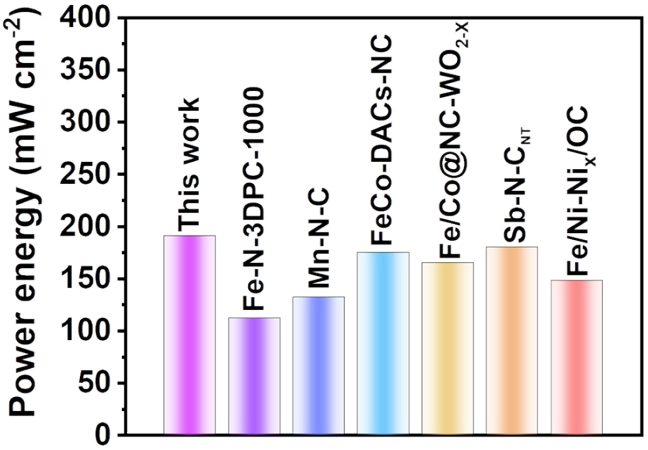

Figure S23. Comparison of the power energy between Re-SAC and the catalysts reported recently.

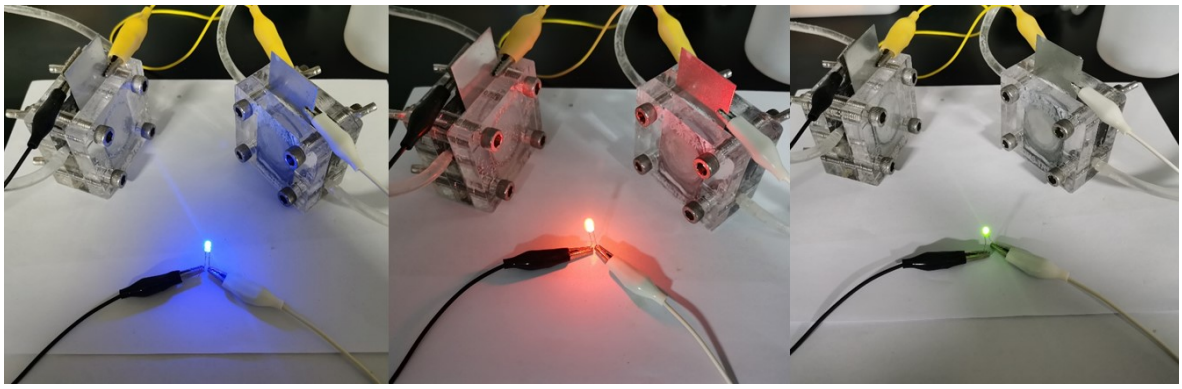

Figure S24. Digital photograph of a commercial color LED (blue, red, and green) lit by two-series-connected Re-SAC-based home-made ZAB.

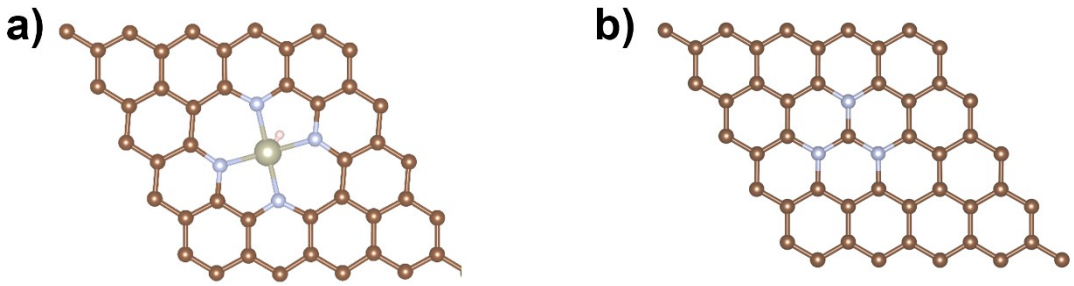

Figure S25. The optimized structure diagrams of (a) Re-SAC and (b) N-C.

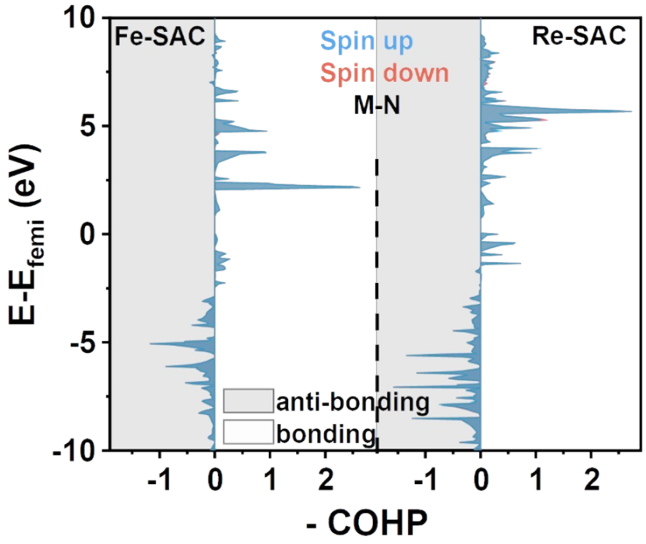

Figure S26. COHP for the M-N (M = Fe or Re) bond in Re-SAC and Fe-SAC.

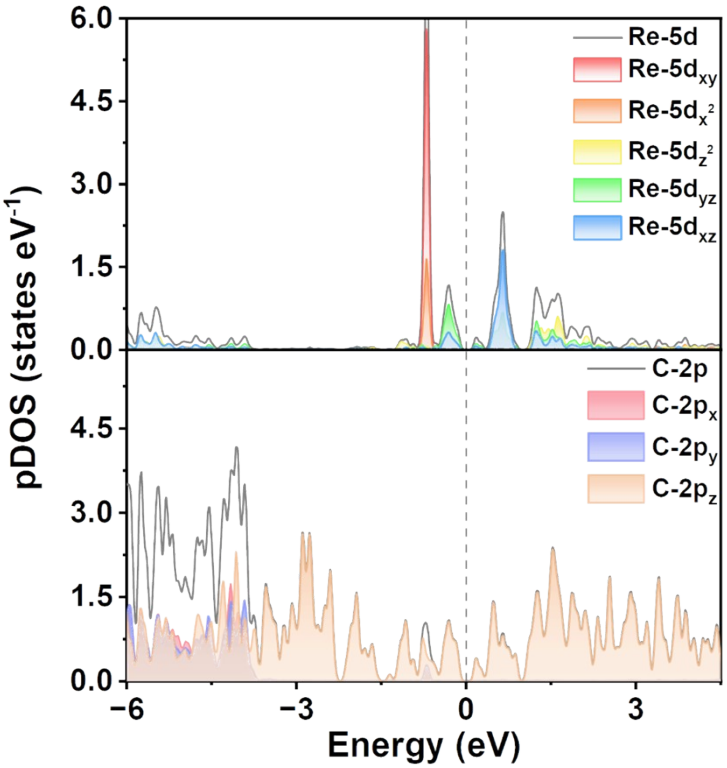

Figure S27. The calculated pDOS of C 2p and Re 5d for Re-SAC.

Table S1. BET surface area, micropore sufface area and mesopore area of Re-SAC and N-C catalysts.

Sample	S_{BET} (m^2 g^{-1})	$S_{micropore}$ (m^2 g^{-1})	$S_{mesopore}$ (m^2 g^{-1})	$S_{micropore}/S_{BET}$
Re-SAC	1582.0	908.6	673.4	57.4 %
N-C	1294.6	868.7	425.9	67.1 %

Considering the crucial importance of microporous sites in controlling catalytic performance and the role of mesoporous sites in enhancing ion transport efficiency, the ratio of $S_{micropore}/S_{BET}$ was utilized as a metric to assess the impact of pore size. According to this key indicator, Re-SAC catalyst with a hierarchically porous structure exhibited remarkable ORR activity.

Table S2. Structural parameters extracted from the Re L_3-edge EXAFS fitting (S_0^2 = 0.899).

Sample	Shell	*CN*[a]	*R*(Å)[b]	σ^2(Å^2)[c]	ΔE_0(eV)[d]	*R* factor
Re foil	Re-Re	12	2.74	0.0033	7.8	0.0001
Re-SAC	Re-N(O)	3.7	1.72	0.0083	6.1	0.0018
	Re-N(O)	0.3	2.08	0.0083		

[a]*CN*: coordination numbers; [b]*R*: bond distance; [c]σ^2: Debye-Waller factors; [d]ΔE_0: the inner potential correction. *R* factor: goodness of fit. S_0^2 was set to 0.899, according to the experimental EXAFS fit of Re foil by fixing CN as the known crystallographic value.

Table S3. The ORR performance comparison of Pt/C in this work with the reported values in literature.

Catalyst	E_{onset} (V)	$E_{1/2}$ (V)	Tafel plots (mV dec^{-1})	References
Pt/C	0.96	0.85	79	This work
Pt/C	1.01	0.86	92	*Angew. Chem. Int. Ed.* 2024, **63**, e202316314[S2]
Pt/C	0.997	0.874	95	*Energy Environ. Sci.* 2023,**16**, 3576-3586[S3]
Pt/C	0.93	0.85	61	*J. Am. Chem. Soc.* 2024, 146, **13**, 9124-9133[S4]
Pt/C	0.94	0.83	68	*Adv. Mater.* 2024, **36**, 2400523[S5]
Pt/C	0.96	0.85	71	*Adv. Funct. Mater.* 2024, **34**, 2311664[S6]
Pt/C	0.94	0.84	81	*Adv. Funct. Mater.* 2023, **33**, 2300405[S7]
Pt/C	1.00	0.85	66	*Angew. Chem. Int. Ed.* 2024, **63**, e202402657[S8]
Pt/C	0.95	0.88	76	*Energy Environ. Sci.* 2024,**17**, 2298-2308[S9]
Pt/C	0.96	0.89	70	*Angew. Chem. Int. Ed.* 2024, **63**, e202316005[S10]
Pt/C	0.90	0.834	96	*Energy Environ. Sci.* 2022,**15**, 1601-1610[S11]
Pt/C	0.93	0.83	90	*Carbon,* 2021, **171**, 1-9[S12]
Pt/C	0.95	0.84	90	*Nano Energy* 2021, **87,** 106153[S13]
Pt/C	0.95	0.85	90	*Angew. Chem. Int. Ed.,* 2022, **61**, e202114441[S14]
Pt/C	0.97	0.74	81	*Energy Environ. Sci.* 2023,**16**, 2629-2636[S15]
Pt/C	0.92	0.84	84	*Energy. Environ. Sci.* 2018, **11**, 2263-2269[S16]
Pt/C	0.95	0.87	74	*Energy Environ. Sci.* 2023,**16**, 4464-4473[S17]
Pt/C	0.96	0.87	84	*Energy Environ. Sci.* 2024,**17**, 704-716[S18]
Pt/C	0.93	0.85	100	*Angew. Chem. Int. Ed.* 2023, **89**, e202308344[S19]
Pt/C	0.98	0.85	74	*Adv. Sci.* 2022, **9**, 2104237[S20]
Pt/C	0.98	0.872	67	*Adv. Mater.* 2020, **32**, 2004670[S21]

Table S4. ORR performance comparison of Re-SAC with other highly active catalysts reported recently.

Catalyst	Electrolyte	Onset potential	Half-wave potential	Peak power density (mW cm^{-2})	Reference
V-N-C	0.1 M KOH	0.95 V	0.86 V	-	[S12]
Fe-N-3DPC-1000	0.1 M KOH	0.90 V	0.87 V	112	[S13]
Ru-SAS/SNC	0.1 M KOH	1.00 V	0.86 V	-	[20]
Fe-NCS	0.1 M KOH	0.92 V	0.88 V	-	[S22]
Se SA@NC	0.1 M KOH	0.95 V	0.85 V	-	[S23]
Co-N-CB	0.1 M KOH	0.90 V	0.87 V	-	[S24]
W SAs/WNNC	0.1 M KOH	0.89 V	0.83 V	-	[S25]
Cu-N-C	0.1 M KOH	0.89V	0.87 V	-	[S16]
Mn-N-C	0.1 M KOH	0.98 V	0.87 V	132	[S26]
FeCo-DACs/NC	0.1 M KOH	0.98 V	0.88 V	175	[S27]
Fe SAs-Fe_2P NPs/NPCFs-2.5	0.1 M KOH	1.03 V	0.91 V	-	[S28]
Fe-Cu-N-mC	0.1 M KOH	0.99 V	0.92 V	-	[S29]
Fe/Co@NC-WO_{2-x}	0.1 M KOH	0.93 V	0.87 V	165	[S30]
Sb-N-C_{NT}	0.1 M KOH	0.96 V	0.88 V	180	[S31]
Fe/Ni-N_x/OC	0.1 M KOH	0.91 V	0.85 V	148	[S32]
Re SAC	0.1 M KOH	0.85 V	0.72 V	-	[S33]
Re-SAC	**0.1 M KOH**	**1.00 V**	**0.89 V**	**191**	**This work**

Table S5. Collection efficiency determined by voltammograms recorded at various rotation speeds using RRDE.

Catalyst	Rotation speed (rpm)	i_{Ring} (mA cm^{-2})	i_{Disk} (mA cm^{-2})	N
No catalyst	925	2.35	-6.39	0.3678
	1600	3.10	-8.37	0.3703
	2025	3.33	-9.03	0.3688
Re-SAC	925	2.35	-6.37	0.3689
	1600	3.00	-8.13	0.3690
	2025	3.38	-9.13	0.3702

Supplementary references

[S1] H. Jin, X. Liu, P. An, C. Tang, H. Yu, Q. Zhang, H. J. Peng, L. Gu, Y. Zheng, T. Song, K. Davey, U. Paik, J. Dong and S. Z. Qiao, *Nat. Commun.,* 2023, **14**, 354.

[S2] X. Feng, G. Chen, Z. Cui, R. Qin, W. Jiao, Z. Huang, Z. Shang, C. Ma, X. Zheng, Y. Han and W. Huang, *Angew. Chem. Int. Ed.,* 2024, **63**, e202316314

[S3] S. Wu, S. Jiang, S.-Q. Liu, X. Tan, N. Chen, J.-L. Luo, S. H. Mushrif, K. Cadien and Z. Li, *Energy Environ. Sci.,* 2023, **16**, 3576-3586.

[S4] H. Li, W. Wang, S. Xue, J. He, C. Liu, G. Gao, S. Di, S. Wang, J. Wang, Z. Yu and L. Li, *J. Am. Chem. Soc.,* 2024, **146**, 9124-9133.

[S5] H. Zhang, H.-C. Chen, S. Feizpoor, L. Li, X. Zhang, X. Xu, Z. Zhuang, Z. Li, W. Hu, R. Snyders, D. Wang and C. Wang, *Adv. Mater.,* 2024, **36**, 2400523.

[S6] Y. Chen, J. Mao, H. Zhou, L. Xing, S. Qiao, J. Yuan, B. Mei, Z. Wei, S. Zhao, Y. Tang and C. Liu, *Adv. Funct. Mater.,* 2024, **34**, 2311664.

[S7] J. Quílez-Bermejo, S. García-Dalí, A. Daouli, A. Zitolo, R. L. S. Canevesi, M. Emo, M. T. Izquierdo, M. Badawi, A. Celzard and V. Fierro, *Adv. Funct. Mater.,* 2023, **33**, 2300405.

[S8] L. Zhao, Y. Dai, Y. Zhang, B. Liu, P. Guo, Z. Zhang, L. Shen, N. Zhang, Y. Zheng, Z. Zhang, Z. Wang and Z. Chen, *Angew. Chem. Int. Ed.,* 2024, **63**, e202402657.

[S9] C. Chen, J. Chai, M. Sun, T. Guo, J. Lin, Y. Zhou, Z. Sun, F. Zhang, L. Zhang, W. Chen and Y. Li, *Energy Environ. Sci.*, 2024, **17**, 2298-2308.

[S10] X. Shu, D. Tan, Y. Wang, J. Ma and J. Zhang, *Angew. Chem. Int. Ed.*, 2024, **63**, e202316005.

[S11] H. Li, S. Di, P. Niu, S. Wang, J. Wang and L. Li, *Energy Environ. Sci.*, 2022, **15**, 1601-1610.

[S12] Y. Huang, K. Liu, S. Kan, P. Liu, R. Hao, W. Liu, Y. Wu, H. Liu, M. Liu and K. Liu, *Carbon*, 2021, **171**, 1-9.

[S13] C. Shi, Y. Liu, R. Qi, J. Li, J. Zhu, R. Yu, S. Li, X. Hong, J. Wu, S. Xi, L. Zhou and L. Mai, *Nano Energy*, 2021, **87**, 106153.

[S14] H. Hu, J. Wang, B. Cui, X. Zheng, J. Lin, Y. Deng and X. Han, *Angew. Chem. Int. Ed.*, 2022, **61**, e202114441.

[S15] Y. Li, Y. Ding, B. Zhang, Y. Huang, H. Qi, P. Das, L. Zhang, X. Wang, Z.-S. Wu and X. Bao, *Energy Environ. Sci.*, 2023, **16**, 2629-2636.

[S16] F. Li, G.-F. Han, H.-J. Noh, S.-J. Kim, Y. Lu, H. Y. Jeong, Z. Fu and J.-B. Baek, *Energy Environ. Sci.*, 2018, **11**, 2263-2269.

[S17] E. Hua, S. Choi, S. Ren, S. Kim, G. Ali, S. J. Kim, W.-S. Jang, S. Joo, J. Zhang, S. Ji, Y. S. Cho, J. Kang, T. Song, S. Hong, H. Choi, Y.-M. Kim, H. Han and S. W. Kim, *Energy Environ. Sci.*, 2023, **16**, 4464-4473.

[S18] H. Meng, B. Wu, D. Zhang, X. Zhu, S. Luo, Y. You, K. Chen, J. Long, J. Zhu, L. Liu, S. Xi, T. Petit, D. Wang, X.-M. Zhang, Z. J. Xu and L. Mai, *Energy Environ. Sci.*, 2024, **17**, 704-716.

[S19] C. Qi, H. Yang, Z. Sun, H. Wang, N. Xu, G. Zhu, L. Wang, W. Jiang, X. Yu, X. Li, Q. Xiao, P. Qiu and W. Luo, *Angew. Chem. Int. Ed.*, 2023, **62**, e202308344.

[S20] Q. Han, X. Zhao, Y. Luo, L. Wu, S. Sun, J. Li, Y. Wang, G. Liu and Z. Chen, *Adv. Sci.*, 2022, **9**, 2104237.

[S21] Z. Zhu, H. Yin, Y. Wang, C.-H. Chuang, L. Xing, M. Dong, Y.-R. Lu, G. Casillas-Garcia, Y. Zheng, S. Chen, Y. Dou, P. Liu, Q. Cheng and H. Zhao, *Adv. Mater.*, 2020, **32**, 2004670.

[S22] X. Li, Y. Yan, X. Zheng, Y. Yao, Y. Liu, *Chem. Eng. J.,* 2022, **444**, 136363.

[S23] H. Hu, J. Wang, B. Cui, X. Zheng, J. Lin, Y. Deng, X. Han, *Angew. Chem. Int. Ed.,* 2022, **61**, e202114441.

[S24] W. Zhu, Y. Pei, Y. Liu, J. Zhang, Y. Qin, Y. Yin, M.D. Guiver, *ACS Appl. Mater. Interfaces* 2020, **12**, 32842-32850.

[S25] Y. Ma, Y. Yu, J. Wang, J. Lipton, H.N. Tan, L. Zheng, T. Yang, Z. Liu, X.J. Loh, S.J. Pennycook, L. Shen, Z. Kou, A.D. Taylor, J. Wang, *Adv. Sci.,* 2022, **9**, 2105192.

[S27] Y. Wang, X. Zhang, S. Xi, X. Xiang, Y. Du, P. Chen, D. Lyu, S. Wang, Z.Q. Tian, P.K. Shen, *ACS Sustain. Chem. Eng.,* 2020, **8**, 9367-9376.

[S28] M. Liu, N. Li, S. F. Cao, X. M. Wang, X. Q. Lu, L. J. Kong, Y. H. Xu, X. H. Bu, *Adv. Mater.,* 2022, **34**, 2107421.

[S29] Y. Pan, X. L. Ma, M. M. Wang, X. Yang, S. J. Liu, H-C. Chen, Z. W. Zhuang, Y. H. Zhang, W. C. Cheong, C. Zhang, X. Cao, R. Shen, Q. Xu, W. Zhu, Y. Q. Liu, X. D. Wang, X. J. Zhang, W. S. Yan, J. Li, H. M. Chen, C. Chen, Y. D. Li, *Adv. Mater.,* 2022, **34**, 2203621.

[S30] C. H. Qi, H. Y. Yang, Z. Q. Sun, H. F. Wang, N. Xu, G. H. Zhu, L. J. Wang, W. Jiang, X. Q. Yu, X. P. Li, Q. Xiao, P. P. Qiu, W. Luo, *Angew. Chem. Int. Ed.,* 2023, **89**, e202308344.

[S31] D. Zhang, X. Xie, P. P. Sun, Y. A. Wei, T. Gong, N. Huang, X. W. Lv, L. Fang, X. H. Sun,

Chem. Eng. J., 2022, **439**, 135700.

[S32] Z. J. Zhu, H. J. Yin, Y. Wang, C. H. Chuang, L. Xing, M. Y. Dong,Y. R. Lu, G. C. Garcia, Y. L. Zheng, S. Chen, Y. H. Dou, P. Liu, Q. L. Cheng, H. J. Zhao, *Adv. Mater.,* 2020, **32**, 2004670.

[S33] X. H. Zhang, S. Lu, Z. J. Yang, T. R. Zhang, *ChemPlusChem,* 2021, **86**, 1635-1639.